

Generalised model-independent characterisation of strong gravitational lenses V: lensing distance ratio in a general Friedmann universe

Jenny Wagner¹ and Sven Meyer²

¹ Universität Heidelberg, Zentrum für Astronomie, Astron. Rechen-Institut, Mönchhofstr. 12–14, 69120 Heidelberg, Germany

² Universität Heidelberg, Zentrum für Astronomie, Institut für Theoretische Astrophysik, Philosophenweg 12, 69120 Heidelberg, Germany
e-mail: {j.wagner, sven.meyer}@uni-heidelberg.de

Received XX; accepted XX

ABSTRACT

Context. Determining the cosmic expansion history from a sample of supernovae of type Ia, data-based cosmic distance measures can be set up that make no assumptions about the constituents of the universe, i.e. about a specific cosmological model. The overall scale, usually determined by the Hubble constant H_0 , is the only free parameter left.

Aims. We investigate to which accuracy and precision the lensing distance ratio D of our distance to the lens, to the source, and their relative distance can be determined from the most recent Pantheon sample. Subsequently inserting D and its uncertainty into the gravitational lensing equations for given H_0 , esp. the time-delay equation between a pair of multiple images, allows to determine lens properties, esp. differences in the lensing potential ($\Delta\phi$), without specifying a cosmological model. Alternatively, given $\Delta\phi$ between a pair of multiple images, e.g. by a lens model, H_0 can be determined.

Methods. We expand the luminosity distances into an analytic orthonormal basis, determine the maximum-likelihood weights for the basis functions by a globally optimal χ^2 -parameter estimation, and derive confidence bounds by MCMC sampling. To detect over-, underfitting, and biases of a basis, we set up quality criteria based on the reduced χ^2 and the Fisher information, and test whether the inaccuracies are encompassed in the confidence bounds. In this way, we assess and compare four analytic bases that resemble distances in Einstein-de-Sitter and Λ CDM models.

Results. For typical strong gravitational lensing configurations between $z = 0.5$ and $z = 1.0$, we find that $\Delta\phi$ can be determined with a relative imprecision of 1.7%, assuming imprecisions of the time delay and the redshift of the lens on the order of 1%. Using a Λ CDM model, the relative imprecision of $\Delta\phi$ is 1.4%. Minimum relative imprecisions for H_0 amount to 20% and 10% for galaxy- and galaxy-cluster-scale lenses when including measurements of velocity dispersions in a single-lens-plane model.

Conclusions. With only a small, tolerable loss in precision, the model-independent lens characterisation developed in this paper series can be generalised by dropping the specific Friedmann model to determine D in favour of a data-based distance ratio. Moreover, for any astrophysical application, the approach presented here, provides distance measures up to $z = 2.3$ that are valid in any homogeneous, isotropic universe with general relativity as theory of gravity.

Key words. cosmology: distance scale – gravitational lensing: strong – gravitational lensing: weak – methods: analytical – stars: supernovae: general

1. Introduction

1.1. Motivation from previous works

There is hardly any astrophysical research question that does not involve the distance to an object of interest. While distance measurements in our galactic neighbourhood can be performed to high precision and accuracy, Gaia Collaboration et al. (2018), extra-galactic distance measurements become increasingly difficult, Cuesta et al. (2015); Muraveva et al. (2014); Tegmark (2002). Thus, with the development of an observation-based cosmic distance ladder still ongoing, cosmic distances are usually inferred from a measured (spectroscopic or photometric) redshift in combination with a cosmological model that assigns the redshift to a cosmic distance. So far, the cosmological standard model, as most precisely measured by Planck Collaboration et al. (2018), is inserted into these distance measures.

As one example, in the gravitational lensing formalism, angular diameter distances between the observer and the lens D_l , the observer and the source D_s , and the distance between the lens and the source D_{ls} appear in the lensing equations to scale the (multiple) images, the source, and the deflection potential with respect to each other. The so-called lensing distance ratio

$$D(z_l, z_s) = \frac{D_l D_s}{D_{ls}}, \quad (1)$$

appears, for instance, in the time delay τ_{ij} between two multiple images i and j of the same background galaxy located at angular position \mathbf{y} in the source plane, which is given by

$$\tau_{ij} = D \frac{(1+z_l)}{c} (\phi(\mathbf{y}, \mathbf{x}_i) - \phi(\mathbf{y}, \mathbf{x}_j)) \equiv D \frac{(1+z_l)}{c} \Delta\phi. \quad (2)$$

\mathbf{x}_i are the measured angular positions of the two images in the lens plane and $\phi(\mathbf{y}, \mathbf{x})$ is the lensing potential; c denotes the speed

of light and z_1 the redshift of the lens. The lensing potential is given by

$$\phi(\mathbf{x}, \mathbf{y}) = \frac{1}{2} (\mathbf{x} - \mathbf{y})^2 - \psi(\mathbf{x}), \quad (3)$$

in which $\psi(\mathbf{x})$ denotes the projected, two-dimensional gravitational deflection potential of the lens in the lens plane. A detailed introduction of the gravitational lensing formalism can be found, e.g. in Petters et al. (2001); Schneider et al. (1992).

In the previous four papers of this series, Wagner (2017); Wagner & Tessore (2018); Wagner (2018a,b), we investigated gravitational lensing from a model-independent perspective. We derived equations that determine local lens properties for different configurations of multiple images solely from observed properties of these images without assuming a specific model for the lens and determined invariance transformations of these equations to derive the degeneracies in our ansatz. As the next step of generalisation of this ansatz, we now replace the distance measures based on a cosmological model by data-based distance measures. Since most lenses and their background sources are located at redshifts between $z = 0$ to $z = 2.0$, reconstructing their distances by a supernova sample, like the Pantheon sample, Scolnic et al. (2018), is possible. Hence, we can obtain data-based distances for most lensing configurations without the need to calibrate several probes of the cosmic expansion with respect to each other.

The paper is organised as follows: in the remainder of this section, we discuss related work on the usage of supernovae to reconstruct the cosmic expansion history. Then, Section 2 gives a brief introduction into cosmological model building based on Friedmann universes and discusses the observational prerequisites and basics of the standardisation of supernovae that influence the reconstructions of the cosmic expansion and distance measures. As the Pantheon sample (contrary to its antecessors) is not calibrated by an overall scale, we derive the equations to reconstruct the expansion function from a scale-free sample. Having obtained a normalised expansion function, we insert it into the definitions of distance measures to obtain data-based luminosity and angular diameter distances. In Section 3, the implementational details of the approach are given, before it is applied to the Pantheon sample and a Pantheon-like simulation in Section 4. We use H_0 as derived from cosmic-microwave background measurements or as measured in our local neighbourhood and show their deviations in the results. In addition to evaluating the accuracy and the precision of our implementation, we also compare our Friedmann-parameter-free reconstructions of the expansion function, the luminosity distances, and the lensing distance ratio to the ones of Λ CDM models, as parametrised by Planck Collaboration et al. (2016)¹ and Scolnic et al. (2018). In Section 5, we compare the precision of the lensing distance ratio to the precision of the other observables entering the time-delay equation of two multiple images of the same background source to estimate the loss of precision when dropping the parametrisation of the Friedmann model in favour of a data-based distance measure. We also show the usage of the Friedmann-parameter-free distances to derive H_0 from measurements of time delays. Our approach simplifies the determination of H_0 because it does not require to marginalise over many possible cosmological models, for instance, like different dark energy models. Section 6 summarises the results, discusses the advantages and disadvantages of Friedmann-parameter-free distance measures and gives an outlook for further applications.

¹ being the most recent data release at the time of performing our experiments

1.2. Related work of supernovae Ia as cosmological probes

The idea to reconstruct the evolution of the cosmic density (perturbations) from luminosity distances of standardisable candles goes back to Starobinsky (1998) and has been employed in many ways and variants since then. The basic ansatz solves

$$D_L(a) = \frac{c}{a} \int_a^1 \frac{dx}{x^2 H(x)} \quad (4)$$

for $H(a)$ having measured the luminosity distance $D_L(a)$ from the observer to supernovae at the left-hand side and assuming that the universe is flat. Tegmark (2002) extended and detailed the original idea and suggested combinations of different probes of the cosmic density. Huterer & Turner (1999) provided first feasibility tests for different dark energy potentials by Monte-Carlo simulations.

Depending on their way, how to invert Equation (4), several approaches are distinguished. Shafieloo et al. (2006) contains a detailed list of approaches, therefore, we focus on more recent ones here: Direct methods reconstruct $H(a)$ from the smoothed or averaged version of the original data set, e.g. as done in Shafieloo et al. (2006); Shafieloo (2007); Wang & Tegmark (2005). Basis-function methods reconstruct $H(a)$ by expanding $D_L(a)$, the distance modulus μ , $H(a)$, or a parametrisation thereof, into a set of basis functions, e.g. as done in Gómez-Valent & Amendola (2018); Ishida & de Souza (2011); Mignone & Bartelmann (2008). Bayesian methods reconstruct $H(a)$ either employing Gaussian processes or other priors, e.g. as done in Gómez-Valent & Amendola (2018); Porqueres et al. (2017); Seikel et al. (2012), and the most recently by Lemos et al. (2018) (and references therein).

In addition, other ansatzes exist that use supernovae of type Ia as cosmic probes, e.g. the ones by Seikel & Schwarz (2008, 2009) that establish a model-independent hypothesis test to reject the hypothesis that the universe is not expanding.

We base our approach on Mignone & Bartelmann (2008) that has been further investigated in Benitez-Herrera et al. (2012, 2013) because, from all of the above, it seems to be most suitable for reconstructing cosmic distances, in particular for the lensing distance ratio D , as will be further detailed in Section 2 and 3, and tested in Section 4.

2. Theoretical derivations

2.1. Cosmological model prerequisites

Assuming that our universe is spatially homogeneous and isotropic on large scales, the line element ds can be parametrised as

$$ds^2 = \sum_{i,j=0}^3 g_{ij} dx_i dx_j = -c^2 dt^2 + a(t)^2 d\mathbf{x}^2, \quad (5)$$

in which g_{ij} denotes the components of the metric, c the speed of light, t the cosmic time variable, $a(t)$ the scale factor, and $d\mathbf{x}$ the spatial line element of the three-dimensional hypersurfaces of constant time. The latter can be parametrised as

$$d\mathbf{x}^2 = dr^2 + f_K^2(r) (\sin^2(\theta) d\phi^2 + d\theta^2) = dr^2 + f_K^2(r) d\Omega^2 \quad (6)$$

in spherical coordinates $\mathbf{x} = (r, \phi, \theta)$ (with the solid angle line element $d\Omega$) due to the spherical symmetry that is implied by isotropy. Furthermore, the symmetry assumptions require the

three-dimensional spatial hypersurfaces to be spaces of constant curvature K , such that the function $f_K(r)$ can be parametrised by

$$f_K(r) = \begin{cases} \frac{\sinh(\sqrt{|K|}r)}{\sqrt{|K|}} & \text{for } K < 0 \\ r & \text{for } K = 0 \\ \frac{\sin(\sqrt{K}r)}{\sqrt{K}} & \text{for } K > 0 \end{cases}. \quad (7)$$

Inserting Equations (6) and (7) into Equation (5), we obtain the components of the Robertson-Walker metric.

If, in addition, gravitation in this universe can be described by general relativity, inserting the Robertson-Walker metric (RW metric) into Einstein's field equations yields the Friedmann equations. Any RW metric whose scale factor $a(t)$ fulfils the Friedmann equations is called a Friedmann-Lemaître-Robertson-Walker metric (FLRW metric). In this work, we are only interested in the first order Friedmann equation,

$$H(t)^2 \equiv \left(\frac{\dot{a}(t)}{a(t)}\right)^2 = \frac{8\pi G}{3}\rho - \frac{Kc^2}{a^2} + \frac{\Lambda c^2}{3}, \quad (8)$$

in which G denotes the gravitational constant, $-\rho c^2$ the zero-zero component of the energy-momentum tensor on the right-hand side of Einstein's field equations, and Λ the cosmological constant. The dot denotes the derivative with respect to cosmic time t . Without loss of generality, we choose the scale factor today to be one, $a_0 \equiv a(t_0) = 1$, in order to determine a uniquely.

Being agnostic about the constituents and the state of the universe (i.e. not knowing anything about ρ , K , or Λ), we can generally define

$$H(a) \equiv H_0 E(a), \quad (9)$$

calling $H(a)$ the Hubble function of the universe with the expansion function $E(a)$ and today's Hubble constant $H_0 = H(a_0)$. Thus, $E(a)$ is normalised, such that $E(a_0) = 1$. Splitting the constituents into radiation, matter, curvature and a Λ -term, we arrive at the usual parametrisation of the Hubble function

$$H(a) = H_0 \sqrt{\Omega_{r0} a^{-4} + \Omega_{m0} a^{-3} + \Omega_K a^{-2} + \Omega_\Lambda}, \quad (10)$$

with Ω_i being today's density divided by the critical density.

With the help of Equation (9) and the distance duality relation of Etherington (1933), we can calculate the luminosity and the angular diameter distances between two scale factors a_1 and a_2 with $a_2 < a_1$, as

$$D_L(a_1, a_2) = \frac{c}{H_0} \frac{a_1}{a_2} f_K \left(\int_{a_2}^{a_1} \frac{dx}{x^2 E(x)} \right), \quad (11)$$

$$D_A(a_1, a_2) = \frac{c}{H_0} \frac{a_2}{a_1} f_K \left(\int_{a_2}^{a_1} \frac{dx}{x^2 E(x)} \right) = \left(\frac{a_2}{a_1}\right)^2 D_L(a_1, a_2). \quad (12)$$

2.2. Observational prerequisites

In order to employ Equations (11) and (12) to reconstruct $H(a)$, observations from standardisable candles, rulers, or sirens can be used. For supernovae of type Ia, determining D_L by fitting their light curves to standardised templates has become a routine (see e.g. Amanullah et al. (2010); Betoule et al. (2014); Burns et al.

(2011); Scolnic et al. (2018); Suzuki et al. (2012)). Light curve fitters, like SALT2 (Guy et al. (2010)), determine

$$D_L = 10^{\frac{\mu}{5} + 1}, \quad (13)$$

in which the distance modulus μ is a function of the observed light curves (usually measured as magnitudes in the b -band), the absolute magnitude M for a standardised supernova of type Ia, and parameters of the light curve fitter to correct for biases, e.g. in the distance modulus due to the host-galaxy mass of the individual supernovae. The impact of these biases is calibrated by simulations that may depend on an underlying Friedmann model with a special parametrisation. Thorough analyses have been performed that investigate the dependence of the inferred quantities, e.g. μ or cosmological parameters, on the trained and calibrated light-curve model, see Mosher et al. (2014) and Haurer et al. (2018), and enhanced simulations that employ several parametrised Friedmann models for the calibration and blind the light curve fitting with respect to a reference cosmology, have been established, Kessler & Scolnic (2017).

Setting Equation (13) equal to (11) and inserting Equation (10) into the latter, cosmological parameter values can be retrieved. Usually, nuisance parameters like the absolute magnitude M are fitted together with the cosmological parameters². M and H_0 both define an overall scale for the distances and are thus not independent of each other. Since the light-curve standardisation is performed without fixing M , observations of supernovae only determine $E(a)$ without constraining the overall distance scale. This has to be set by one of the following options:

- scaling with a measurement of H_0 , e.g. from Planck Collaboration et al. (2016) or from Riess et al. (2018), or
- a measurement of M for supernovae in our local neighbourhood, Richardson et al. (2014) or
- employing Bayesian statistics to infer cosmological parameter values after having marginalised over the prior probability of all nuisance parameters, e.g. assuming a non-informative prior probability distribution for M (which is not pursued in this work).

In our work, we use the most recent Pantheon sample from Scolnic et al. (2018), which provides $\mu + M$ from a compilation of $N_D = 1048$ supernovae between $a_{\min} = 0.307$ and $a_{\max} = 0.990$ as data. Basing on the frequentist framework of statistics for the remainder of this work, we reconstruct the normalised expansion function, $E(a)$, from these supernovae and subsequently scale with H_0 from Planck Collaboration et al. (2016). This seems to be the most consistent approach because observations of local supernovae properties might be subject to small-scale anisotropy biases that are not included in the FLRW metric from which we derive $E(a)$ and the distance measures (see e.g. Planck Collaboration et al. (2016) for a detailed discussion about the tension of currently available measurements of H_0 and Marra et al. (2013), Bolejko (2018), and Macpherson et al. (2018) for recent advances to reconcile the measurements from the cosmic microwave background and the local neighbourhood). Vice versa, using the $E(a)$ as reconstructed from the Pantheon sample to determine H_0 from time-delay measurements according to Equation (2) contributes to resolving the tension between the different H_0 -values currently proposed (see Section 5).

² Determining M for different, redshift-dependent subsets, as performed in Suzuki et al. (2012), revealed that all M are in good agreement with each other. Thus, a single scale M for the entire data set is sufficient.

2.3. Scale-free series expansion of D_L

We define the luminosity distance function $D_L(a, \mathbf{c})$ as an expansion into orthonormal basis functions $\phi_\alpha(a)$

$$D_L(a, \mathbf{c}) = \sum_{\alpha=0}^{N_B-1} c_\alpha \phi_\alpha(a) = \mathbf{c} \circ \Phi \quad (14)$$

for $a \in [a_{\min}, 1]$, in which the c_α denote the weights of the basis functions and each entry in $\mathbf{c} \in \mathbb{R}^{N_B}$ is multiplied by the respective column in $\Phi \in \mathbb{R}^{N_D \times N_B}$ and these terms are summed up in the short-hand notation of the right hand side. This ansatz has also been pursued in Benitez-Herrera et al. (2012, 2013); Mignone & Bartelmann (2008). Since, apart from some minor restrictions detailed in Appendix A, $D_L(a, \mathbf{c})$ can be exactly represented in any basis, we do not insert a specific one until Section 3.1.

Denoting the data as provided by Scolnic et al. (2018) as $d_i \equiv d(a_i) = \mu_i + M$, we factor out the unknown overall scale in Equation (13) as

$$D_{L,i} = 10^{\frac{H_i}{5}+1} = 10^{\frac{d_i-M}{5}+1} \equiv 10^{-\frac{M}{5}} \tilde{D}_{L,i}, \quad \forall i = 1, \dots, N_D. \quad (15)$$

In order to link Equations (14) and (15), we define

$$D_L(a, \mathbf{c}) = 10^{-\frac{M}{5}} \tilde{D}_L(a, \tilde{\mathbf{c}}) = 10^{-\frac{M}{5}} \tilde{\mathbf{c}} \circ \Phi. \quad (16)$$

Given the covariance matrix between the d_i (including systematic correlations), $\Sigma_\mu \in \mathbb{R}^{N_D \times N_D}$, we obtain the entries of the scale-free covariance matrix for D_L , $\tilde{\Sigma}$, by calculating

$$\Sigma_{ij} = D_{L,i} D_{L,j} k_\Sigma = 10^{-\frac{2M}{5}} \tilde{D}_{L,i} \tilde{D}_{L,j} k_\Sigma \quad (17)$$

$$\equiv 10^{-\frac{2M}{5}} \tilde{\Sigma}_{ij}, \quad \forall i, j = 1, \dots, N_D \quad (18)$$

with

$$k_\Sigma = \left(10^5 \frac{\Sigma_{\mu,ij}}{\sqrt{\Sigma_{\mu,ii}} \sqrt{\Sigma_{\mu,jj}}} + \frac{\Sigma_{\mu,ij}}{5 \sqrt{\Sigma_{\mu,jj}}} - 10^5 \frac{\Sigma_{\mu,ij}}{\sqrt{\Sigma_{\mu,ii}}} - 10^5 \frac{\Sigma_{\mu,ij}}{\sqrt{\Sigma_{\mu,jj}}} + 1 \right). \quad (19)$$

A derivation of Σ_{ij} can be found in Appendix B.

To obtain the \mathbf{c} in Equation (14) from Equation (15), we set up a generalised linear-least-squares parameter estimation as

$$\arg \min_{\mathbf{c}} \chi^2 = \arg \min_{\mathbf{c}} \left\{ (\mathbf{D}_L - \mathbf{D}_L(a, \mathbf{c}))^\top \Sigma^{-1} (\mathbf{D}_L - \mathbf{D}_L(a, \mathbf{c})) \right\}, \quad (20)$$

in which $\mathbf{D}_L = (D_{L,1}, \dots, D_{L,N_D})^\top$ denotes the column vector of the luminosity distance measurements and $\mathbf{D}_L(a, \mathbf{c})$ is the column vector containing the luminosity distances at the same a as determined by Equation (14)³.

Inserting Equations (15), (16), and (18) into Equation (20), we obtain

$$\chi^2 = (\tilde{\mathbf{D}}_L - \tilde{\mathbf{D}}_L(a, \tilde{\mathbf{c}}))^\top \tilde{\Sigma}^{-1} (\tilde{\mathbf{D}}_L - \tilde{\mathbf{D}}_L(a, \tilde{\mathbf{c}})). \quad (21)$$

Hence, the scaled and scale-free optimisation problems, and thus, their solutions, are of the same form and yield the unbiased, consistent, efficient, and asymptotically normal generalised least-squares estimator⁴

$$\hat{\mathbf{c}} = (\Phi^\top \Sigma^{-1} \Phi)^{-1} (\Phi^\top \Sigma^{-1}) \mathbf{D}_L = 10^{-\frac{M}{5}} \hat{\tilde{\mathbf{c}}}. \quad (22)$$

³ This ansatz assumes that the errors in a are negligible, which is realised by incorporating the uncertainties and biases in the redshift measurements in the covariance matrix Σ_μ , see Betoule et al. (2014).

⁴ under the assumption that $\mathbb{E}[\mathbf{D}_L - \mathbf{D}_L(a, \mathbf{c}) | \mathbf{D}_L] = 0$

If the deviations of \mathbf{D}_L to $\mathbf{D}_L(a, \mathbf{c})$ are normally distributed, it is also the maximum-likelihood estimator. For the sake of convenience, unless specified otherwise, we will drop the tilde and refer to the scale-free solution as $\hat{\mathbf{c}}$.

Compared to other methods that expand $E(a)$ in a set of basis functions, the ansatz pursued in Equation (14) has the advantage that it is easy to show that Equation (20) has a single global optimum which can be efficiently determined by Equation (22).

2.4. Reconstruction of the Hubble function

Luminosity distances of supernovae are measured with respect to $a = 1$ today. Hence, when inserting $D_L(a, \hat{\mathbf{c}})$ on the left-hand side of Equation (11), we also have to insert $a_1 = 1$ and $a_2 = a$ on the right-hand side. If not explicitly specified, we abbreviate $D_L(a) \equiv D_L(1, a)$ for the luminosity distance defined by Equation (11) and analogously for the angular diameter distance measure.

Following Starobinsky (1998), we can solve Equation (11) for $E(a)$ by first isolating the integral of the right-hand side

$$\int_a^1 \frac{dx}{x^2 E(x)} = f_K^{-1} \left(\frac{H_0}{c} a D_L(a) \right), \quad (23)$$

subsequently deriving both sides by a

$$-\frac{1}{a^2 E(a)} = \frac{H_0}{c} \frac{\partial f_K^{-1} \left(\frac{H_0}{c} a D_L(a) \right)}{\partial \left(\frac{H_0}{c} a D_L(a) \right)} \left(D_L(a) + a \frac{dD_L(a)}{da} \right) \quad (24)$$

and then obtain $E(a)$ as

$$E(a) = - \left[a^2 \frac{H_0}{c} \frac{\partial f_K^{-1} \left(\frac{H_0}{c} a D_L(a) \right)}{\partial \left(\frac{H_0}{c} a D_L(a) \right)} \left(D_L(a) + a \frac{dD_L(a)}{da} \right) \right]^{-1}. \quad (25)$$

We restrict the discussion to flat universes with $K = 0$, so that $f_K(r) = r$, which is in agreement with the measurements of Planck Collaboration et al. (2016). The cases for non-vanishing curvature are analogous and treated in Appendix C for the sake of completeness.

Inserting $D_L(a, \hat{\mathbf{c}})$ for $D_L(a)$ into Equation (25), we obtain the expansion function up to an overall scale, $\tilde{E}(a)$. If the supernova sample were calibrated such that $c/H_0 = 10^{-M/5}$, the reconstructed expansion function would be normalised, $\tilde{E}(a) = E(a)$. Hence, inserting the data-based scale-free series expansion $\tilde{D}_L(a, \hat{\mathbf{c}})$ into Equation (25), we obtain a normalised expansion function by

$$E(a) = \frac{\tilde{E}(a)}{\tilde{E}(a_{\max})}. \quad (26)$$

Inserting $\tilde{D}_L(a, \hat{\mathbf{c}})$ and its derivative into Equation (25), dropping all scale factors, and normalising the result, $E(a)$ is given by

$$E(a) = - \left[a^2 \tilde{E}(a_{\max}) \hat{\mathbf{c}} \circ \left(\Phi + a \frac{d\Phi}{da} \right) \right]^{-1}. \quad (27)$$

Consequently, when introducing the overall scale to determine $H(a)$, we use

$$H(a) = H(a_{\max}) E(a). \quad (28)$$

Since, for the Pantheon sample, $a_{\max} = 0.99 \approx 1$ and $H(a_{\max}) = 68.06$ km/s/Mpc for the Planck cosmological parameters (Planck Collaboration et al. (2016)) is contained in the confidence interval of $H_0 = 67.74 \pm 0.46$ km/s/Mpc, we may also approximate $H(a_{\max})$ by H_0 in Equation (28).

Since the basis functions can be determined at all $a \in [a_{\min}, 1]$ (either analytically or numerically), Equations (27) and (28) yield a data-based expansion and Hubble function at any $a \in [a_{\min}, 1]$.

2.5. Reconstruction of distances

Inserting Equation (28) into Equations (11) or (12), we can now determine distances between arbitrary scale factors without specifying a parametrisation like in Equation (10).

If an unbiased, global measurement of an absolute distance for a standardised supernova M were available, we could simply insert M into Equation (16) and solve Equation (20) for \hat{e} (i.e. the scaled quantity as defined on the left-hand side of Equation (22)) to determine data-based distance measures. As we will briefly show in Section 4.4, this would lead to a higher degree of accuracy and tighter confidence bounds. Until such a measurement might become feasible, Sections 4.3 and 4.4 show that employing Equations (11) or (12) with (28) currently is the most robust way to determine data-based distances.

2.6. Reconstruction of the lensing distance ratio

With the establishment of data-based distance measures as detailed in Section 2.5, we can determine the lensing distance ratio for all lenses and sources located within the redshift⁵ range of the reconstruction, as defined in Equation (1). In Sections 4.3 and 4.4, we will specify a lens redshift z_1 and calculate the lens distance ratio for all sources at $z_s > z_1$.

3. Implementational details

3.1. Analytic bases

3.1.1. Einstein-de-Sitter basis

As a set of orthonormal basis functions, we use the Einstein-de-Sitter basis as introduced in Mignone & Bartelmann (2008). It consists of functions

$$u_\alpha(a) = a^{\frac{\alpha}{2}-1}, \quad \alpha = 0, \dots, N_B - 1, \quad (29)$$

that are recursively orthonormalised over the scale factor interval $[a_{\min}, 1]$ by Gram-Schmidt orthonormalisation to obtain the $\phi_\alpha(a)$ introduced in Equation (14). This basis is designed to recover the luminosity distances in an Einstein-de-Sitter universe ($\Omega_{m0} = 1, \Omega_\Lambda = 0$) with the first two basis functions. It is thus a sparse basis decomposition in the matter-dominated era of the cosmic evolution, for scale factors approximately ranging from $a \approx 10^{-3}$ to $a \approx 0.7$.

3.1.2. Variations of the Einstein-de-Sitter basis

In the late universe ($a \gtrsim 0.7$), the term of the cosmological constant, Ω_Λ , dominates in Equation (10) and the universe expands

⁵ While we use a as variable for the reconstructions of the Hubble function and the distance measures, we convert a to the redshift z for the reconstruction of D to be consistent with standard lensing notation.

exponentially. Determining the luminosity distances, then yields $D_L(a) \propto 1/a^2 - 1/a$, such that a basis obtained from

$$u_\alpha(a) = a^{\alpha-2}, \quad \alpha = 0, \dots, N_B - 1 \quad (30)$$

is physically motivated analogously to the one obtained from Equation (29).

Since Equation (30) does not include the square-root functions contained in Equation (29), a combination of both bases can be obtained from functions of the form

$$u_\alpha(a) = a^{\frac{\alpha}{2}-2}, \quad \alpha = 0, \dots, N_B - 1. \quad (31)$$

For the reconstruction of $H(a)$, it turns out that the term in the last bracket of Equation (25) belonging to c_0 cancels out when using the Einstein-de-Sitter basis. This implies that the Hubble function is effectively reconstructed by $N_B - 1$ basis functions and coefficients, such that we also set up a modified Einstein-de-Sitter basis without the first basis function from functions of the form

$$u_\alpha(a) = a^{\frac{\alpha-1}{2}}, \quad \alpha = 0, \dots, N_B - 1. \quad (32)$$

Table 1 summarises the functions that form the basis sets of Sections 3.1.1 and 3.1.2 after Gram-Schmidt orthonormalisation and also lists the first four functions that are employed to set up the bases.

Table 1. Parameter-free, analytic, orthonormal basis function sets used in this work.

Basis	Name	$u_\alpha(a)$	$u_0(a)$	$u_1(a)$	$u_2(a)$	$u_3(a)$
1	EdS	$a^{\alpha/2-1}$	$1/a$	$1/\sqrt{a}$	1	\sqrt{a}
2	Λ	$a^{\alpha-2}$	$1/a^2$	$1/a$	1	a
3	comp	$a^{\alpha/2-2}$	$1/a^2$	$1/\sqrt{a^3}$	$1/a$	$1/\sqrt{a}$
4	mod	$a^{(\alpha-1)/2}$	$1/\sqrt{a}$	1	\sqrt{a}	a

3.2. Further numerical bases

Even sparser bases that require fewer coefficients for the reconstruction exist, e.g. the principal component basis as introduced in Ishida & de Souza (2011) or Maturi & Mignone (2009). Yet, these approaches are less suitable for our purpose than an analytic basis. The latter assumes a physically motivated decomposition into basis functions that can be efficiently determined at any arbitrary point between $[a_{\min}, a_{\max}]$, while the numerical bases require to be represented by a lot of sampling points. The dense sampling increases the run-time. It also requires numerical imprecisions to be carefully taken into account and an interpolation between the sampling points to be defined (see Section 4.4 for a comparison of a numerical and the analytic implementation of the Einstein-de-Sitter basis). Apart from requiring a high accuracy and precision in the lens ratio distance, the increasing amount of data in a data set with an increasing interval of scale factors also requires a fast reconstruction of $H(a)$ and the distance measures. This favours closed form expressions over numerical ones, especially when the confidence bounds are determined by Markov-Chain-Monte-Carlo sampling as detailed in Section 3.3.

3.3. Confidence bounds

The uncertainties on \hat{c} due to the covariances of the $D_{L,i}$ are determined by Markov-Chain-Monte-Carlo sampling from the χ^2 in Equation (21): We simulate 1000 data sets with N_D SNe, each at the same scale factors as are listed in the original data set by drawing $D_{L,i}$, $i = 1, \dots, N_D$ from a Gaussian distribution around the measured $D_{L,i}$ with a width σ corresponding to the measured uncertainty as listed in the original data set. Correlations between different data points are neglected because we focus on the imprecision that is caused by the measurement uncertainties in the $D_{L,i}$. The correlations that arise due to the compilation of several inhomogeneous data sets to one are usually much smaller than the statistical uncertainties. For the Pantheon sample, we find that the correlations, i.e. the off-diagonal entries, in Σ_μ are all smaller than 1% of the statistical uncertainties.

For each of the 1000 simulated data sets, $E(a)$, $D_L(a)$, and $D(z_1, s)$ are reconstructed. From the ensemble of all 1000 reconstructions of each quantity, the 68%, 95% and 99% confidence intervals, corresponding to $1\text{-}\sigma$, $2\text{-}\sigma$ and $3\text{-}\sigma$ confidence intervals for a Gauss distribution are calculated. In addition, we determine the standard deviation of each quantity from the 1000 simulated data sets.

3.4. Quality assessment of a basis

A priori, a Friedmann-parameter-free reconstruction of $E(a)$, $D_L(a)$, and $D(z_1, z_s)$ can be performed with any set of orthonormal basis functions. To rank and compare different bases with different number of basis functions, N_B , we introduce the following criteria to assess their reconstruction quality:

- the reduced χ^2 defined as

$$\chi_v^2 \equiv \frac{\chi^2}{N_D - N_B}, \quad (33)$$

- the Cramér-Rao bound on the covariance of the estimator of coefficients \hat{c} as detailed below,
- the relative inaccuracy of the reconstruction of a Pantheon-like simulated data set,
- the relative imprecision of the reconstruction given by the confidence bounds determined according to Section 3.3.

The optimal reconstruction has $\chi_v^2 = 1$ and an inaccuracy smaller than the imprecision, so that the measurement uncertainties dominate potential systematic biases. If $\chi_v^2 > 1$, the basis does not fully capture the information contained in the data or the covariances have been underestimated. For $\chi_v^2 < 1$, the basis overfits the data or the covariances have been overestimated.

To derive the quality assessment by the Cramér-Rao bound, we assume a multivariate normal distribution of the deviations of $D_{L,i}$ from $D_L(a, \hat{c})$ (see Section 2.3). Then, the Fisher information matrix is given by

$$\mathcal{I}(\mathbf{c}) = \Phi^\top \Sigma^{-1} \Phi \in \mathbb{R}^{N_B \times N_B}. \quad (34)$$

Given the unbiased estimator \hat{c} for the vector of coefficients, the Cramér-Rao bound states that the covariance of \hat{c} , $\text{cov}(\hat{c})$, is bounded from below as

$$\text{cov}(\hat{c}) \geq \mathcal{I}^{-1}(\mathbf{c}), \quad (35)$$

which means that $(\text{cov}(\hat{c}) - \mathcal{I}^{-1}(\mathbf{c}))$ is positive semi-definite.

Inserting the covariance matrix from the MCMC sampling (drawn from a Gaussian distribution with covariance matrix

Σ) for $\text{cov}(\hat{c})$ and determining the Fisher information matrix from the same covariance matrix, Σ , we can calculate $(\text{cov}(\hat{c}) - \mathcal{I}^{-1}(\mathbf{c}))$. Thus, we can rank the different bases by the distance of this matrix difference to zero

$$|d_I| \equiv |\text{cov}(\hat{c}) - \mathcal{I}^{-1}(\mathbf{c})|. \quad (36)$$

As measure for this distance, $|\cdot|$ denotes the absolute value of the largest eigenvalue of $(\text{cov}(\hat{c}) - \mathcal{I}^{-1}(\mathbf{c}))$. Furthermore, the deviation from positive semi-definiteness indicates whether \hat{c} could be biased. Assuming a bias $\mathbf{b}(\mathbf{c}) \in \mathbb{R}^{N_B}$ that changes the estimator \hat{c} to $\mathbf{T}(\mathbf{c}) = \mathbf{c} + \mathbf{b}(\mathbf{c}) \in \mathbb{R}^{N_B}$, the Cramér-Rao bound becomes

$$\text{cov}(\hat{c}) \geq \left(\frac{\partial \mathbf{T}(\mathbf{c})}{\partial \mathbf{c}} \right) \mathcal{I}^{-1}(\mathbf{c}) \left(\frac{\partial \mathbf{T}(\mathbf{c})}{\partial \mathbf{c}} \right)^\top, \quad (37)$$

such that negative eigenvalues of $(\text{cov}(\hat{c}) - \mathcal{I}^{-1}(\mathbf{c}))$ hint at a bias.

To summarise, we search for the basis which comes closest to $\chi_v^2 = 1$, has the smallest bias measured by the Cramér-Rao bound and shows the smallest confidence bounds (i.e. relative imprecisions) that encompass the relative inaccuracies at the 68% confidence level.

3.5. Run-time enhancements

Our implementation is based on MATLAB, employing the full covariance matrix including the correlations between the data points. As detailed in Section 4.2, we choose the Einstein-de-Sitter basis as orthonormal set of basis functions. Analytically performing the Gram-Schmidt orthonormalisation, we obtain closed-form expressions for Φ and subsequently closed-form expressions for $D_L(a, \hat{c})$, $H(a)$, $D_L(a)$, and $D(z_1, z_s)$ up to $N_B = 4$. Higher order coefficients and basis functions can be retrieved numerically. Yet, for the Pantheon sample, maximally four coefficients are significantly determined given the covariances (see Section 4.2).

A major speed-up in run-time is obtained by replacing the standard *inv*-function by *mldivide*() to calculate \hat{c} and by replacing all *for*-loops by matrix operations. The overall run-time to reconstruct $H(a)$, $D_L(a)$, and $D(z_1, z_s)$ (the latter for one fixed z_1 , as detailed in Section 2.6) including confidence bounds according to Section 3.3 for the Pantheon sample amounts to roughly 110 seconds on a standard notebook (MacBook Pro, 2.2 GHz Intel Core i7, 8 GB 1333 MHz DDR3 RAM).

4. Application to data

4.1. Synopsis of the data

As observational data, we use the Pantheon data set, Scolnic et al. (2018) for the selection of the optimum basis function (Section 4.2) and to determine the reconstruction precision for $E(a)$, $D_L(a)$, and $D(z_1, z_s)$ (Section 4.3). To investigate the reconstruction accuracies (Section 4.4), we generate Pantheon-like simulations. We simulate luminosity distances at the scale factors of the Pantheon sample from a Λ CDM model as parametrised by Planck Collaboration et al. (2016), based on measurements from the cosmic microwave background, (see first column of Table 2) and divide them by an arbitrary scale to obtain scale-free $\tilde{D}_{L,i}$. The parametrisation in the second row of Table 2 by Scolnic et al. (2018) is based on the Pantheon sample and measurements of H_0 in the local neighbourhood (we employ H_0 from Riess et al. (2018) here). It is used in Section 4.3 and in Section 4.5 for the comparison with model-based reconstructions.

Table 2. Λ CDM parametrisations of Planck Collaboration et al. (2016) (first row) and Scolnic et al. (2018) (second row).

Λ CDM model	Ω_{r0}	Ω_{m0}	Ω_K	Ω_Λ	H_0 [km/s/Mpc]
(Planck)	0.0	0.3089	0.0	0.6911	67.74
(Scolnic)	0.0	0.298	0.0	0.702	73.52 ⁽¹⁾

References. (1) Riess et al. (2018)

4.2. Selection of the optimal basis

We first perform a comparison of the bases listed in Table 1 to find the optimal basis and number of basis functions, N_B , given the quality assessment criteria of Section 3.4. Table 3 shows the quality measures for different configurations of the basis sets. For all bases 1 to 4, we test 2 to 6 numerically implemented basis functions, equidistantly sub-sampled at $N_S = 10000$ points between a_{\min} and 1. We employ the full covariance matrix in Equation 21 and determine confidence bounds as detailed in Section 3.3.

Comparing \hat{c} for basis 1 for all N_B with the \hat{c} obtained when using the diagonal covariance matrix with the statistical uncertainties only, we find that the coefficients deviate only on the order of 10^{-4} . Hence, correlations between the different data in the Pantheon sample play a minor role for the reconstructions of $E(a)$, $D_L(a)$, and $D(z_1, z_s)$.

For all bases, $N_B > 3$ yields χ_v^2 slightly smaller than one, as listed in the third column of Table 3, so that we conclude that these basis configurations capture the information contained in the data well. Contrary to that $N_B = 2$ has $\chi_v^2 > 1$ for all bases, indicating that these configurations are not suitable to represent $D_L(a)$.

In the fourth column of Table 3, we list the Cramér-Rao bound calculated for the full covariance matrix of the Pantheon sample. All basis configurations are biased because the largest eigenvalue is negative such that the matrix $(\text{cov}(\hat{c}) - I^{-1}(c))$ is negative semi-definite. Compared to the entries in $\text{cov}(\hat{c})$ and $I^{-1}(c)$, the largest eigenvalues of the difference can be of the same order of magnitude, so that the bias is not a numerical artefact. Repeating the analysis of the Cramér-Rao bound for the diagonal covariance matrix, we observe that the configurations with $N_B = 3, 6$ are most strongly biased with leading negative eigenvalue. The negative eigenvalues for the other configurations with $N_B = 4, 5$ are at least two orders of magnitude smaller than the largest, positive eigenvalue, which is listed in the fifth column of Table 3. Thus, the correlations between the data are a major source of the bias.

Next, we observe that the relative inaccuracies are contained within the 68%-confidence bounds for configurations of $N_B > 3$ for bases 1, 3, and 4 and for $N_B > 5$ for basis 2. For these configurations, we compare the standard deviations of \hat{c} for all N_B to find the best basis configuration for each of the four basis sets. Since uncertainties grow with increasing number of coefficients, we find the best basis configurations as follows:

- basis 1 with $N_B = 4$,
- basis 2 with $N_B = 5$,
- basis 3 with $N_B = 4$,
- basis 4 with $N_B = 4$.

From those, basis 1 with $N_B = 4$ turns out to have the smallest confidence bounds and thus the least relative imprecision for the reconstructions of $E(a)$, $D_L(a)$, and $D(z_1, z_s)$ from the Pantheon sample. Figure 1 shows the relative inaccuracies of the

Pantheon-like simulation and relative imprecisions for the reconstructions of the Pantheon sample in form of the standard deviations of the MCMC samples as obtained according to Section 3.3. For the plots showing the relative inaccuracies, the model-based reconstructions from Λ CDM (Planck Collaboration et al. (2016)) are subtracted from our reconstructions.

Thus, unless mentioned otherwise, all reconstructions in the following are determined with the standard settings for our MATLAB code as detailed in Section 3, i.e. we employ

- the full scale-free covariance matrix, $\tilde{\Sigma}$ from the Pantheon sample (see Equation (18)),
- the scale-free Einstein-de-Sitter basis of Section 3.1.1 with $N_B = 4$ basis functions (see Equation (16)),
- closed-form expressions for the basis functions, their derivatives to reconstruct $E(a)$, $D_L(a)$, and $D(z_1, z_s)$ (Equations (27), (11), (1)) as detailed in Section 2,
- the scaling according to Equation (28) with $H(a_{\max})$ as determined by the Λ CDM model based on Planck Collaboration et al. (2016),
- 1000 Markov-Chain-Monte-Carlo samples from the Pantheon data set to calculate confidence bounds as detailed in Section 3.3.

4.3. Reconstruction precision from the Pantheon sample

Running the MATLAB code with all specifications as described at the end of Section 4.2, we obtain $E(a)$, $D_L(a)$, and $D(0.5, z_s) \equiv D(z_s)$ as shown in Figure 2 (left column) and the relative reconstruction imprecisions (right column).

We compare our reconstruction to the respective quantities of a Λ CDM model as parametrised by Planck Collaboration et al. (2016) and by Scolnic et al. (2018) as summarised in Table 2. In order to compare $E(a)$ on equal footage, we normalise it to the value at a_{\max} for the Λ CDM models as well.

For $E(a)$, both model-based reconstructions lie well within the confidence bounds of our reconstruction. The same applies to the model-based reconstructions for $D_L(a)$ and $D(0.5, z_s)$ as parametrised by Planck Collaboration et al. (2016). As expected, the tension in H_0 between Planck Collaboration et al. (2016) and Riess et al. (2018) causes the $D_L(a)$ and $D(0.5, z_s)$ as determined by the parametrisation of Scolnic et al. (2018) to lie below the 99% confidence bounds of our reconstruction because the latter is based on H_0 as measured by Planck Collaboration et al. (2016).

4.4. Reconstruction accuracy from simulated data

Having determined the reconstruction precision for the Pantheon sample, we investigate the reconstruction accuracy for a Pantheon-like simulated data set, as detailed in Section 4.1. All remaining input to the reconstruction is taken from the specifications listed at the end of Section 4.2. Figure 3 shows the results. The reconstruction of Λ CDM (Planck Collaboration et al. (2016)) (or of Scolnic et al. (2018)) is subtracted from our reconstruction.

The plot on the left of Figure 3 shows the increase in accuracy for $E(a)$ with an increasing amount of basis functions. For $N_B = 3, 4$, the closed-form basis functions are used, while for $N_B = 5$, we employ the numerical implementation. While reconstructions with $N_B = 3, 4$ favour the parametrisation of Scolnic et al. (2018), for $N_B = 5$ the parametrisation of the underlying simulation of Planck Collaboration et al. (2016) is finally preferred.

Table 3. Quality assessment of the bases of Table 1 according to Section 3.4; (sys) and (stat) denote the Cramér-Rao criterion based on the full covariance matrix and on the diagonal covariance matrix, respectively; the 6th column checks whether the relative imprecision (P) at 68% confidence level is larger than the relative inaccuracy (A), and the remainder lists the \hat{c} and its standard deviation obtained from 1000 MCMC samples.

B	N_B	χ_r^2	d_I (sys)	d_I (stat)	P>A	\hat{c}_0	\hat{c}_1	\hat{c}_2	\hat{c}_3	\hat{c}_4	\hat{c}_5	σ_{c_0}	σ_{c_1}	σ_{c_2}	σ_{c_3}	σ_{c_4}	σ_{c_5}	
1	2	1.5534	-8.03E-8	5.88E-8	✗	0.5658	-0.2402					0.0013	0.0006					
1	3	0.9065	-4.68E-8	-8.07E-7	✗	0.6805	-0.3229	0.0264				0.0045	0.0032	0.0010				
1	4	0.9063	-3.00E-6	6.41E-6	✓	0.6717	-0.3158	0.0217	0.0013			0.0094	0.0083	0.0046	0.0012			
1	5	0.9069	-2.21E-5	2.08E-5	✓	0.6649	-0.3087	0.0162	0.0041	-0.0007		0.0146	0.0144	0.0102	0.0048	0.0012		
1	6	0.9052	-7.96E-6	-2.87E-5	✓	0.6515	-0.2926	-0.0001	0.0169	-0.0076	0.0019	0.0163	0.0169	0.0136	0.0087	0.0042	0.0011	
2	2	1.7080	-2.54E-7	1.54E-7	✗	1.0009	-0.2296					0.0024	0.0006					
2	3	0.9439	-4.41E-7	-9.94E-7	✗	0.8121	-0.1480	-0.0238				0.0069	0.0028	0.0008				
2	4	0.9072	-5.15E-6	9.81E-6	✗	0.7397	-0.1064	-0.0464	0.0061			0.0132	0.0071	0.0036	0.0010			
2	5	0.9070	-2.10E-5	2.14E-5	✓	0.7246	-0.0961	-0.0538	0.0098	-0.0010		0.0191	0.0118	0.0077	0.0035	0.0009		
2	6	0.9050	-8.20E-7	-2.88E-5	✓	0.7060	-0.0810	-0.0679	0.0204	-0.0066	0.0015	0.0212	0.0141	0.0106	0.0066	0.0031	0.0008	
3	2	2.9099	-3.47E-7	1.92E-7	✗	1.1351	-0.2941					0.0028	0.0008					
3	3	0.9144	-1.32E-6	-6.64E-7	✗	0.7629	-0.1150	-0.0511				0.0083	0.0039	0.0011				
3	4	0.9055	-8.74E-6	1.77E-5	✓	0.7179	-0.0858	-0.0668	0.0041			0.0161	0.0098	0.0049	0.0013			
3	5	0.9064	-1.23E-5	1.22E-5	✓	0.7168	-0.0849	-0.0675	0.0045	-0.0001		0.0209	0.0144	0.0094	0.0044	0.0011		
3	6	0.9064	-7.67E-6	-2.24E-5	✓	0.7099	-0.0773	-0.0759	0.0116	-0.0041	0.0011	0.0219	0.0162	0.0126	0.0083	0.0042	0.0011	
4	2	1.5841	-1.50E-7	1.05E-7	✗	0.7229	-0.4075					0.0017	0.0010					
4	3	0.9510	-7.76E-7	-1.93E-6	✗	0.9193	-0.5750	0.0419				0.0076	0.0064	0.0016				
4	4	0.9062	-1.35E-5	2.61E-5	✓	0.8163	-0.4693	-0.0050	0.0105			0.0164	0.0163	0.0068	0.0015			
4	5	0.9064	-2.71E-5	3.00E-5	✓	0.8026	-0.4536	-0.0146	0.0148	-0.0010		0.0229	0.0246	0.0133	0.0053	0.0012		
4	6	0.9062	-1.13E-5	-4.04E-5	✓	0.7925	-0.4393	-0.0273	0.0242	-0.0060	0.0013	0.0244	0.0274	0.0171	0.0098	0.0046	0.0012	

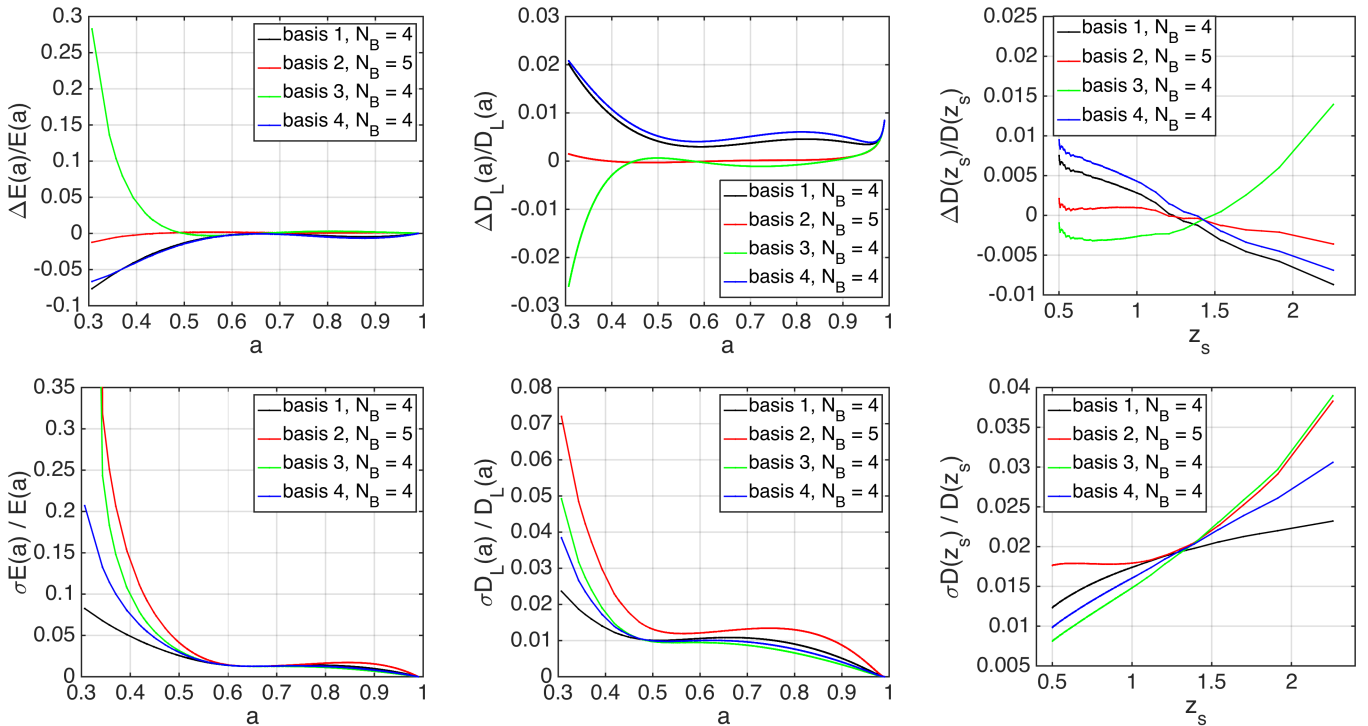


Fig. 1. Top (from left to right): Relative inaccuracies of $E(a)$, $D_L(a)$, and $D(0.5, z_s)$ w.r.t. the ones from a Λ CDM model as parametrised in Planck Collaboration et al. (2016). Bottom (from left to right): Relative imprecisions (standard deviations of the MCMC samples) of $E(a)$, $D_L(a)$, and $D(0.5, z_s)$ for the same basis configurations.

Reconstructing $D_L(a)$ with $N_B = 4$, we compare the implementation with the numerical and the analytic basis functions in the central plot of Figure 3. For small scale factors, the 1% gain in accuracy between the numerical implementation sampled at the scale factors of the Pantheon sample (i.e. Φ is evaluated at $N_S = 1048$ sampling points) and the analytic basis functions can also be achieved for a numerical basis function with $N_S = 10000$ sampling points. Yet, this increases the run-time of the D_L -routine by more than a factor of 4 and still causes numerical instabilities when the scale factor approaches 1.

For the lensing distance ratio D , determined for a typical lens at redshift $z_l = 0.5$ as a representative example, we obtain the relative inaccuracies as shown in the plot on the right-hand side of Figure 3. It shows that the reconstruction with numerical basis functions is slightly worse than the one employing analytic basis functions. In addition, we plot the relative reconstruction inaccuracies that arise when we first reconstruct $\hat{D}_L(a, \hat{e})$ with Equation (16), insert the M as scaling factor that the simulated data has been previously divided by, and subsequently determine D from the $D_L(a, \hat{e})$ (using Equation 12 to convert D_L to D_A to be inserted into Equation (1)). As stated in Section 2.2, using a global measurement of M as scaling would thus yield a higher accuracy for sources close to the lens (for $z_l = 0.5$ the sources should be located between $z_s = 0.5$ and 1).

4.5. Comparison to model-based reconstructions

Next, we compare the confidence intervals of our Friedmann-parameter-free reconstructions with the confidence intervals of the model-based reconstructions parametrised by Planck Collaboration et al. (2016), which is the most precise one, and by Scolnic et al. (2018), based on the Pantheon sample. The parametri-

sations are shown in Table 2, the confidence intervals for the parameters are summarised in Table 4.

Table 4. Confidence intervals of Λ CDM parametrisations of Planck Collaboration et al. (2016) (first row) and Scolnic et al. (2018) (second row) to determine confidence intervals on model-based $E(a)$, $D_L(a)$, and $D(z_l, z_s)$.

Λ CDM model	$\Delta\Omega_{r0}$	$\Delta\Omega_{m0}$	$\Delta\Omega_K$	$\Delta\Omega_\Lambda$	ΔH_0 [km/s/Mpc]
(Planck)	0.0	0.0062	0.0	0.0062	0.46
(Scolnic)	0.0	0.022	0.0	0.020	1.62 ⁽¹⁾

References. (1) Riess et al. (2018)

Since the absolute scale, e.g. H_0 (see Section 2.2), cannot be determined from the supernova sample and is thus subject to the same confidence intervals for all reconstructions, we only focus on the confidence intervals of the Ω_i . Evaluating relative uncertainties, i.e. $\Delta E(a)/E(a)$, $\Delta D_L(a)/D_L(a)$ and $\Delta D(z_s)/D(z_s)$, H_0 cancels out. To determine confidence bounds on $E(a)$ for the parametrisations according to Planck Collaboration et al. (2016) and Scolnic et al. (2018), we employ the definition of $E(a)$ in Equation (9) and draw 1000 MCMC Pantheon-like data sets at the scale factors of the Pantheon sample. Each Pantheon-like data set is generated with a different Friedmann parametrisation ($\Omega_{m0}, \Omega_\Lambda = 1 - \Omega_{m0}$) drawn from a Gaussian distribution around the values listed in Table 2 with a standard deviation given by the confidence intervals shown in Table 4. Confidence intervals for $E(a)$ parametrised by Planck Collaboration et al. (2016) and Scolnic et al. (2018) are then derived from the MCMC sampling in the same way as for the Friedmann-parameter-free reconstruction (see Section 3.3). Subsequently, the confidence intervals on

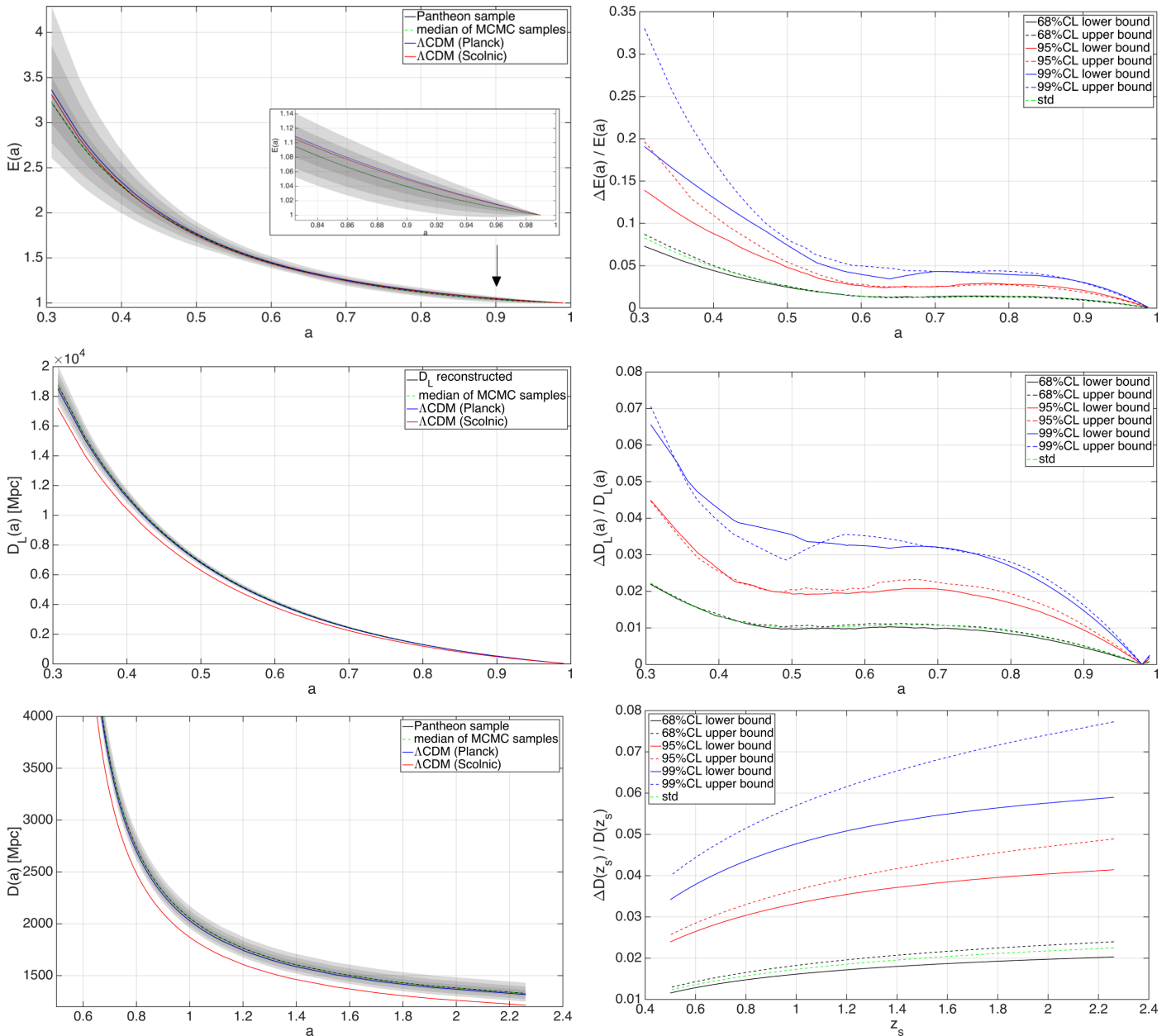


Fig. 2. Top row: $E(a)$ compared to the one from a Λ CDM model as parametrised in Planck Collaboration et al. (2016) and Scolnic et al. (2018) all normalised to $E(a_{\max})$ (left) and its relative reconstruction imprecision (right), Central row: $D_L(a)$ compared to the one from a Λ CDM model as parametrised in Planck Collaboration et al. (2016) and Scolnic et al. (2018) (left) and its relative reconstruction imprecision using the scaling of Equation (28) (right), Bottom row: $D(0.5, z_s)$ based on $D_L(a)$ shown in the central row compared to the one from a Λ CDM model as parametrised in Planck Collaboration et al. (2016) and Scolnic et al. (2018) (left) and its relative reconstruction imprecision (right).

the Λ CDM-parametrised $D_L(a)$ and $D(0.5, z_s)$ are determined. Figure 4 (left) shows the relative imprecision in the reconstructions based on the parametrisation according to Planck Collaboration et al. (2016), Figure 4 (right) shows the same plots for the reconstructions based on the parametrisation according to Scolnic et al. (2018).

We find that the imprecisions for both Λ CDM parametrisations are of the same order with slightly tighter confidence bounds for Planck Collaboration et al. (2016) for $E(a)$ and $D_L(a)$, which is expected from the smaller confidence bounds on Ω_{m0} (see Table 4). For $D(0.5, z_s)$, the width of the confidence intervals for both parametrisations are on equal footing.

As we can observe from a comparison of the plots in Figure 4 with the right-hand side of Figure 2, the precision of $E(a)$

of both model-based reconstructions is about one order of magnitude higher than the Friedmann-parameter-free reconstruction. For $D_L(a)$, the precision of the model-based reconstructions is about a factor of three higher than our reconstruction and for $D(0.5, z_s)$, the model-based reconstruction is about a factor of 25-50 more precise than our reconstruction.

5. Synopsis of results compared to other sources of imprecision in lensing

Summarising the results from Section 4, we find that the lensing distance ratio D for a typical lens redshift z_1 can be reconstructed without specialising a parametrisation for the underlying Friedmann model with a relative imprecision on the order of 1-2%

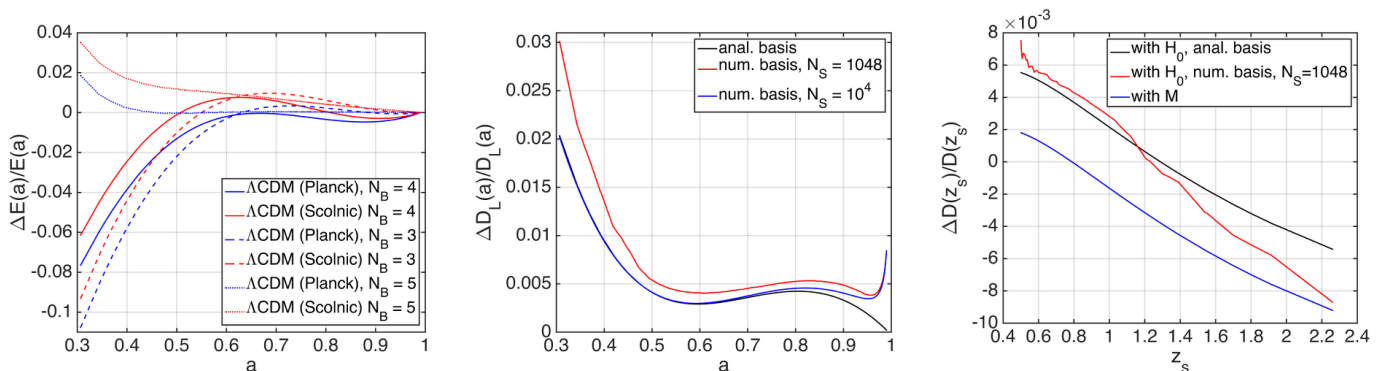


Fig. 3. Left: Relative inaccuracy of $E(a)$ compared to the one from a Λ CDM model as parametrised in Planck Collaboration et al. (2016) and Scolnic et al. (2018) all normalised to $E(a_{\max})$ for $N_B = 3, 4, 5$ basis functions, Centre: Relative inaccuracy of $D_L(a)$ compared to the one from a Λ CDM model as parametrised in Planck Collaboration et al. (2016) for analytic basis functions and numerical basis functions with different number of sampling points, Right: Relative inaccuracy of $D(0.5, z_s)$ based on $D_L(a)$ shown in the centre for a scaling with $H(a_{\max})$ according to Equation (28) and when using a scaling with M according to Equation (16).

(68% confidence level), 2.5-5% (95% confidence level), and 3.5-8% (99% confidence level). Parametrising the Friedmann model with the parameter values of Planck Collaboration et al. (2016) or Scolnic et al. (2018) (see Table 2), the relative imprecisions are below 0.12% for all three confidence levels.

In the model-independent approach to characterise gravitational lenses as developed in Wagner (2017), Wagner & Tessore (2018), and Wagner (2018a) so far, the lensing distance ratio only enters in the time-delay equation, Equation (2), while D does not enter the equations to determine lens properties (locally constrained reduced shear and ratios of potential derivatives) by positions and shapes of multiple images in the lens plane.

5.1. $\Delta\phi$ from Equation (2)

Having measured a time delay between two multiple images, the difference in the lensing potential between those images can be determined with Equation (2). In Wagner (2018a), we showed that time-delay measurements between multiple images fix the enclosed mass density for a given cosmological model, i.e. for a known lensing distance ratio D . Hence, inserting $E(a)$ as reconstructed by the supernovae into Equation (2), we can uniquely determine $\Delta\phi$, given the mathematical prerequisites on ϕ detailed in Wagner (2018a) are fulfilled.

Assuming that the distance and time-delay measurements are performed independently, the relative uncertainty of $\Delta\phi$ is given by

$$\frac{\delta(\Delta\phi)}{\Delta\phi} = \sqrt{\left(\frac{\Delta z_1}{1+z_1}\right)^2 + \left(\frac{\Delta D}{D}\right)^2 + \left(\frac{\Delta\tau_{ij}}{\tau_{ij}}\right)^2}. \quad (38)$$

We estimate the imprecision of the redshift to 1%, considering spectroscopic analysis, as e.g. performed in Scodreggio et al. (2018). Assuming that the time delay is determined between multiple images of quasars, the relative uncertainty amounts to 1-5%. Compared to these estimates, the relative imprecision of D as obtained by our reconstruction is of the same order of magnitude, while the relative imprecision of D obtained by a model-based reconstruction is one order of magnitude smaller, so that

we obtain

$$\left(\frac{\delta(\Delta\phi)}{\Delta\phi}\right)_{PF} \approx \sqrt{(0.01)^2 + (0.01)^2 + (0.01)^2} \approx 1.73\%, \quad (39)$$

$$\left(\frac{\delta(\Delta\phi)}{\Delta\phi}\right)_{PB} \approx \sqrt{(0.01)^2 + (0.001)^2 + (0.01)^2} \approx 1.41\%, \quad (40)$$

where PF and PB stand for our Friedmann-parameter-free (PF) reconstruction and the parametrised Friedmann model (PB), respectively. Hence, generalising the reconstruction of the gravitational lensing potential by not specifying a parametrisation for the Friedmann model, the precision only deteriorates by 0.32%.

5.2. H_0 from Equation (2)

Employing the time-delay measurement to determine H_0 , we require an independently derived value for $\Delta\phi$. Standard approaches to determine H_0 , e.g. as employed in the H0LiCOW project (see Suyu et al. (2017) for an overview) or in Grillo et al. (2018), set up a lens model to determine $\Delta\phi$ from several other multiple image systems, including the host galaxy of the time-varying source, if visible. To account for the formalism-intrinsic and model degeneracies, additional non-lensing information like velocity dispersions along the line of sight are included in the model. Having determined $\Delta\phi$ and having measured τ_{ij} , D is calculated. So far, all approaches rely on

$$\Delta\phi = \frac{1}{2} \left((\mathbf{x}_i - \mathbf{y})^2 - (\mathbf{x}_j - \mathbf{y})^2 \right) - \left(\psi(\mathbf{x}_i) - \psi(\mathbf{x}_j) \right), \quad (41)$$

in which \mathbf{x}_i denotes the position of image i on the celestial sphere, \mathbf{y} is the position of the source in the source plane and $\psi(\mathbf{x})$ is the projected deflection potential of the lens at \mathbf{x} . To simplify the calculations, Gorenstein et al. (1988) already reformulated Equation (41) as

$$\Delta\phi = \frac{1}{2} (\mathbf{x}_i - \mathbf{x}_j)^\top \left(\boldsymbol{\alpha}(\mathbf{x}_i) + \boldsymbol{\alpha}(\mathbf{x}_j) \right) - \left(\psi(\mathbf{x}_i) - \psi(\mathbf{x}_j) \right), \quad (42)$$

such that it becomes independent of the source position. $\boldsymbol{\alpha}(\mathbf{x})$ denotes the deflection angle of the gravitational lens at \mathbf{x} in the lens plane and it is the first derivative of $\psi(\mathbf{x})$ with respect to \mathbf{x} . Inserting Equation (42) into Equation (2), we arrive at a reduced, simplified formulation to determine D and thus H_0 , given our reconstructed $E(a)$, a measured τ_{ij} and the lensing potential difference $\Delta\phi$.

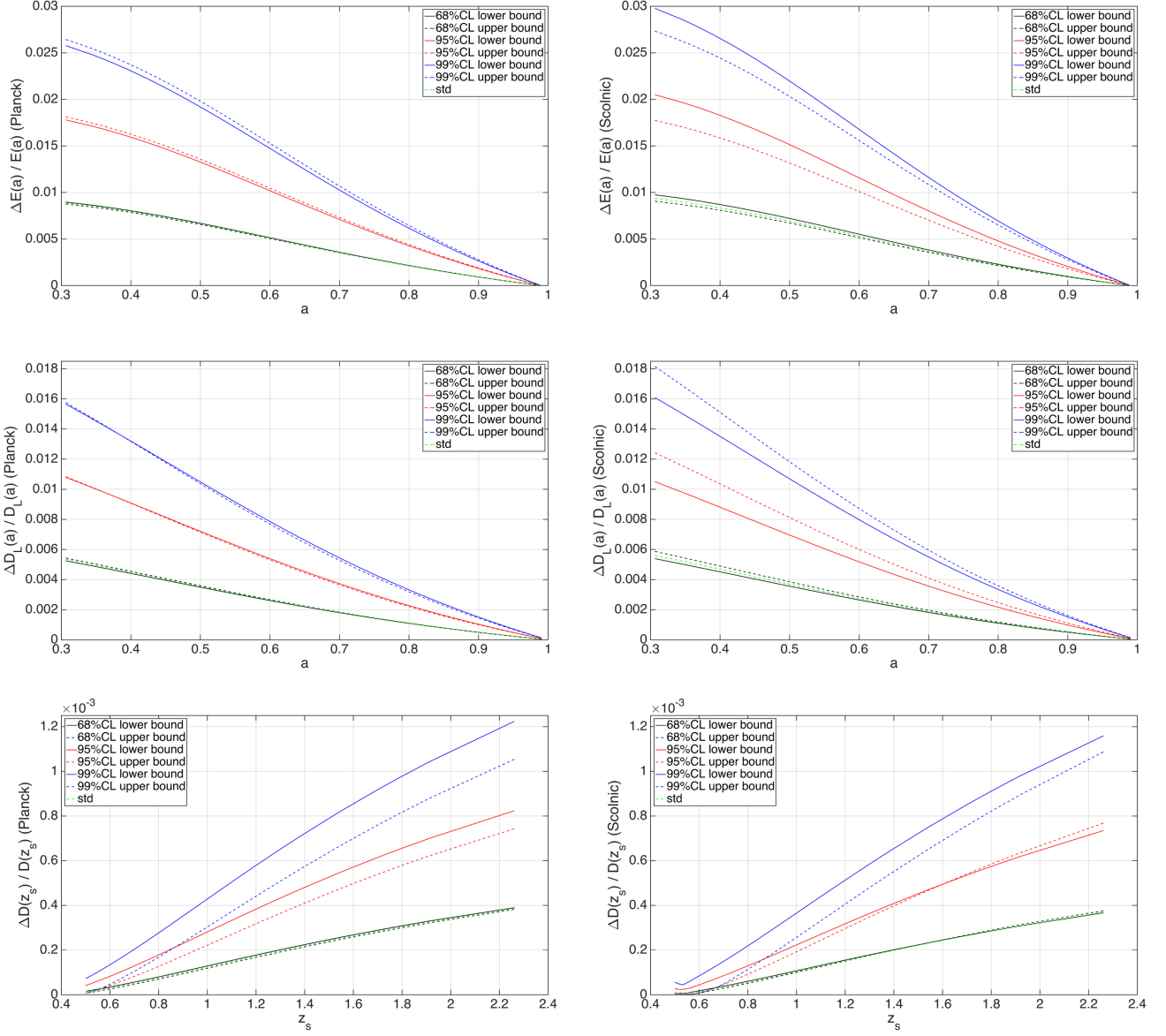


Fig. 4. Left column: Relative imprecisions of $E(a)$, $D_L(a)$, and $D(0.5, z_s)$ for a parametrisation of the Friedmann model according to Planck Collaboration et al. (2016), Right column: Same plots for a parametrisation according to Scolnic et al. (2018).

We note that not every lens model can be used to infer H_0 . For instance, we insert the deflection potential and the deflection angle of a point mass

$$\psi(\mathbf{x}) = \frac{1}{D} \frac{4GM}{c^2} \ln(|\mathbf{x}|), \quad \alpha(\mathbf{x}) = \frac{1}{D} \frac{4GM}{c^2 |\mathbf{x}|}, \quad (43)$$

in which the deflection angle is pointing in radial direction due to the axisymmetry of the configuration. G is the gravitational constant, c the speed of light and M the mass of the lens. Then, the overall factor of $1/D$ of $\Delta\phi$ cancels the D in Equation (2), so that no information on H_0 can be gained in that case. Inserting a singular isothermal sphere, given by

$$\psi(\mathbf{x}) = \frac{D_{\text{ls}}}{D_s} \frac{4\pi\sigma^2}{c^2} |\mathbf{x}|, \quad \alpha(\mathbf{x}) = \frac{D_{\text{ls}}}{D_s} \frac{4\pi\sigma^2}{c^2} \quad (44)$$

into Equation (2), it is obvious that D_1 remains, such that H_0 can be determined. Since σ^2 denotes the velocity dispersion along the line of sight of the deflecting mass distribution, Equation (42)

shows clearly that including additional information breaks degeneracies. In addition, the formulation of Equation (42) allows to factor out functions of distances that are independent of \mathbf{x} for single-plane lens models. This enables us to separate the determination of H_0 from the lens modelling. To estimate the precision to which H_0 can be determined from a general single-plane lens model, we assume the latter can be written as

$$\psi(\mathbf{x}) \equiv f(D) g(p) \tilde{\psi}(\mathbf{x}), \quad (45)$$

in which the distances along the line of sight are given as a function $f(D)$, the additional non-lensing information is given by a function $g(p)$ for the non-lensing information p , and the actual lens model in the lens plane is denoted by $\tilde{\psi}(\mathbf{x})$. Analogously,

$$\alpha(\mathbf{x}) = f(D) g(p) \nabla \tilde{\psi}(\mathbf{x}) \equiv f(D) g(p) \tilde{\alpha}(\mathbf{x}) \quad (46)$$

in which ∇ denotes the gradient with respect to \mathbf{x} . Inserting Equations (45) and (46) into Equation (2), we obtain

$$\tau_{ij} = f(D)Dg(p)\frac{1+z_1}{c}\left(\frac{1}{2}(\mathbf{x}_i - \mathbf{x}_j)^\top(\tilde{\alpha}(\mathbf{x}_i) + \tilde{\alpha}(\mathbf{x}_j)) - \Delta\tilde{\psi}\right) \quad (47)$$

$$\equiv f(D)Dg(p)\frac{1+z_1}{c}\Delta\tilde{\phi}, \quad (48)$$

which can be easily solved for $Df(D)$ and thus for H_0 , if $f(D) \neq 1/D$. Like most lens models, we now set $f(D) = D_{ls}/D_s$ and, using Equation (12), we solve for H_0 to obtain

$$H_0 = \frac{g(p)\Delta\tilde{\phi}}{\tau_{ij}} \int_0^{z_1} \frac{dx}{E(x)} \equiv \frac{g(p)\Delta\tilde{\phi}}{\tau_{ij}} I(z_1, E(z)). \quad (49)$$

Assuming that the individual measurements are independent, the relative uncertainty in H_0 is determined as

$$\frac{\Delta H_0}{H_0} = \sqrt{\left(\frac{\Delta g(p)}{g(p)}\right)^2 + \left(\frac{\Delta(\Delta\tilde{\phi})}{\Delta\tilde{\phi}}\right)^2 + \left(\frac{\Delta\tau_{ij}}{\tau_{ij}}\right)^2 + \left(\frac{\Delta I(E(z))}{I(E(z))}\right)^2}, \quad (50)$$

in which we assumed that the uncertainty in the redshift z_1 is negligible compared to the uncertainty in $E(z)$, so that the relative uncertainty of $I(z_1, E(z))$ is the same as the uncertainty in D_1 . The latter is the same as the uncertainty in the luminosity distance, as shown in Figure 2 under these assumptions. For lenses at $z_1 \leq 1$ ($a \geq 0.5$), the relative uncertainty in the distance to the lens is about 1%. For galaxy-scale lenses, the relative uncertainty in the time delay measured for quasars is of the same order of magnitude, while for galaxy-cluster-scale lenses, it could be about a factor of ten lower, since time delays are increased by approximately the same factor (see Wagner et al. (2018) for a recent overview of time-delay precisions for different transient sources). Measurements of velocity dispersions (usually entering quadratically, as in Equation (44)) have uncertainties on the order of 10% for galaxies and about 5% for galaxy clusters. Thus, the additional non-lensing information and the lens model are the largest sources of uncertainty:

$$\left(\frac{\Delta H_0}{H_0}\right)_g = \sqrt{(2 \cdot 0.1)^2 + \left(\frac{\Delta(\Delta\tilde{\phi})}{\Delta\tilde{\phi}}\right)^2 + (0.01)^2 + (0.01)^2} \quad (51)$$

$$\geq 20.05\%, \quad (52)$$

$$\left(\frac{\Delta H_0}{H_0}\right)_c = \sqrt{(2 \cdot 0.05)^2 + \left(\frac{\Delta(\Delta\tilde{\phi})}{\Delta\tilde{\phi}}\right)^2 + (0.001)^2 + (0.01)^2} \quad (53)$$

$$\geq 10.05\%, \quad (54)$$

in which the subscript g denotes the relative uncertainty for galaxy-scale lenses and c for cluster-scale lenses, respectively. The lower bound on the relative uncertainty for H_0 from the measured quantities alone is 20.05% for galaxy-scale lenses and 10.05% for galaxy-cluster-scale lenses, omitting the term for the lens model in Equation (50).

6. Conclusion

We investigated to which precision and accuracy it is possible to determine the lensing distance ratio $D = D_1 D_s / D_{ls}$ in a generalised Friedmann universe being agnostic about its constituents and their individual contributions. Using the latest compilation of supernovae, the Pantheon sample (Scolnic et al. (2018)), D

can be reconstructed for any combination of lens and source redshifts in the range of 0 to 2.3 with a relative uncertainty on the order of percent. To arrive at this result, we expanded the luminosity distance into a set of orthonormal basis functions. Due to the limited amount of supernovae and their uncertainties, relative inaccuracies in the reconstructed D arise, which lie within the 68% confidence bounds of the measurement uncertainties when we use an Einstein-de-Sitter basis, as introduced in Mignone & Bartelmann (2008), with 4 basis functions. Compared to three other orthonormal basis sets obtained from analytic functions, the Einstein-de-Sitter basis was shown to be the optimal basis set: It has the tightest confidence bounds that encompasses the relative inaccuracies and shows only a slight overfitting and bias in the reconstruction.

Compared to model-based reconstructions of D based on the parametrisations of the Λ CDM model by Planck Collaboration et al. (2016) and Scolnic et al. (2018), our Friedmann-parameter-free reconstruction is a factor of 25-50 less precise than the model-based reconstructions for typical lens and source redshifts between redshifts of 0.5 and 1.0. Yet, propagating the uncertainties through the time-delay equation to determine the difference in the lensing potential between the two multiple images, $\Delta\phi$, we find that $\Delta\phi$ is less than 0.5% less precise for the Friedmann-parameter-free reconstruction than for a Λ CDM model by Planck Collaboration et al. (2016) or Scolnic et al. (2018). This holds for the typical redshift and time-delay uncertainties on the order of percent that are assumed to be the same for the Friedmann-parameter-free and the parametrised reconstructions.

Thus, for the model-independent characterisation of gravitational lensing configurations, we conclude that dropping the parametrisation of the Friedmann model in the lensing distance ratio D in favour of a data-based reconstruction allows us to greatly generalise the method at the cost of a small and tolerable additional imprecision. As a drawback, configurations with redshifts larger than 2.3 cannot benefit from Friedmann-parameter-free lensing distance ratios yet and may require the combination of several cosmic probes.

As a second application, we estimated the relative uncertainty in H_0 that can be determined from a measured time delay, a general single-lens-plane model that includes measurements of the velocity dispersion of the lens, and our reconstruction of $E(a)$. As a lower bound, we find a relative uncertainty of 20% for galaxy-scale lenses and 10% for galaxy-cluster-scale lenses. Improving the precision of the velocity dispersion measurements will greatly reduce the relative uncertainty in H_0 , while the relative uncertainties arising due to the reconstruction of $E(a)$ and the time-delay measurement are about one order of magnitude smaller. Assuming that high-precision measurements of the velocity dispersions of less than 5% relative uncertainty are available, our estimate for the lower bound on the relative uncertainty in H_0 is comparable to the 1- σ confidence bounds in H_0 recently determined in Birrer et al. (2018); Grillo et al. (2018); Wong et al. (2017) using a Bayesian ansatz.

The usage of the reconstructed $E(a)$, $D_L(a)$, $D_A(a)$ is not limited to applications in strong and weak gravitational lensing, distances that are determined from a data-based expansion function can also be employed in any kind of astrophysical context. Furthermore, the Friedmann-parameter-free reconstruction of $E(a)$ can be used to determine the linear growth factor, as done in Haude et al. (2018), and both, $E(a)$ and the linear growth factor are extensively used in the recently developed approach by Bartelmann et al. (2017) to set up propagators for particles moving in the phase space of an expanding universe.

A parametrised Friedmann model yields a higher reconstruction precision, yet, there is a plethora of possible parametrisations that cannot be excluded by current observations, e.g. different types of dark energy or modified gravity models, as summarised e.g. in Amendola et al. (2013) and investigated, e.g. in Benitez-Herrera et al. (2012). We have already analysed the analogous situation in the previous papers of this series for the case of specifying a gravitational lens model. Hence, when considering specific parametrisations of Friedmann models, we should – analogously to specifying gravitational lens models – marginalise over all possible parametrisations to obtain the confidence bounds that represent our knowledge most realistically.

Acknowledgements. We would like to thank Matthias Bartelmann, Sophia Haude, Bettina Heinlein, Bruno Leibundgut, Henrik Nersisyan, Dan Scolnic, and the Galaxy Cluster Group at the Institute for Theoretical Astrophysics for helpful discussions and comments. JW gratefully acknowledges the support by the Deutsche Forschungsgemeinschaft (DFG) WA3547/1-3. SM gratefully acknowledges the support by the Deutsche Forschungsgemeinschaft (DFG) BA 1359 / 20-1.

References

- Amanullah, R., Lidman, C., Rubin, D., et al. 2010, *ApJ*, 716, 712
Amendola, L., Appleby, S., Bacon, D., et al. 2013, *Living Reviews in Relativity*, 16, 6
Bartelmann, M., Fabis, F., Kozlikin, E., et al. 2017, *New Journal of Physics*, 19, 083001
Benitez-Herrera, S., Ishida, E. E. O., Maturi, M., et al. 2013, *MNRAS*, 436, 854
Benitez-Herrera, S., Röpke, F., Hillebrandt, W., et al. 2012, *MNRAS*, 419, 513
Betoule, M., Kessler, R., Guy, J., et al. 2014, *A&A*, 568, A22
Birrer, S., Treu, T., Rusu, C. E., et al. 2018, *ArXiv e-prints* [arXiv:1809.01274]
Bolejko, K. 2018, *Phys. Rev. D*, 97, 103529
Burns, C. R., Stritzinger, M., Phillips, M. M., et al. 2011, *AJ*, 141, 19
Cuesta, A. J., Verde, L., Riess, A., & Jimenez, R. 2015, *MNRAS*, 448, 3463
Etherington, I. M. H. 1933, *Philosophical Magazine*, 15
Gaia Collaboration, Brown, A. G. A., Vallenari, A., et al. 2018, *A&A*, 616, A1
Gómez-Valent, A. & Amendola, L. 2018, *J. Cosmology Astropart. Phys.*, 4, 051
Gorenstein, M. V., Falco, E. E., & Shapiro, I. I. 1988, *ApJ*, 327, 693
Grillo, C., Rosati, P., Suyu, S. H., et al. 2018, *ApJ*, 860, 94
Guy, J., Sullivan, M., Conley, A., et al. 2010, *A&A*, 523, A7
Haude, S., Maturi, M., & Bartelmann, M. 2018, in prep.
Hauret, C., Magain, P., & Biernaux, J. 2018, *MNRAS*, 479, 3996
Huterer, D. & Turner, M. S. 1999, *Phys. Rev. D*, 60, 081301
Ishida, E. E. O. & de Souza, R. S. 2011, *A&A*, 527, A49
Kessler, R. & Scolnic, D. 2017, *ApJ*, 836, 56
Landau, H. J. 1967, *Acta Mathematica*, 117, 37
Lemos, P., Lee, E., Efstathiou, G., & Gratton, S. 2018, *MNRAS*[arXiv:1806.06781]
Macpherson, H. J., Lasky, P. D., & Price, D. J. 2018, *ApJ*, 865, L4
Marra, V., Amendola, L., Sawicki, I., & Valkenburg, W. 2013, *Physical Review Letters*, 110, 241305
Maturi, M. & Mignone, C. 2009, *A&A*, 508, 45
Mignone, C. & Bartelmann, M. 2008, *A&A*, 481, 295
Mosher, J., Guy, J., Kessler, R., et al. 2014, *ApJ*, 793, 16
Muraveva, T., Clementini, G., & Palmer, M. 2014, in *EAS Publications Series*, Vol. 67, *EAS Publications Series*, 275–278
Petters, A. O., Levine, H., & Wambsganss, J. 2001, *Singularity theory and gravitational lensing* (Birkhäuser (Progress in mathematical physics; v. 21))
Planck Collaboration, Ade, P. A. R., Aghanim, N., et al. 2016, *A&A*, 594, A13
Planck Collaboration, Aghanim, N., Akrami, Y., et al. 2018, *ArXiv e-prints* [arXiv:1807.06209]
Porqueres, N., Enßlin, T. A., Greiner, M., et al. 2017, *A&A*, 599, A92
Richardson, D., Jenkins, III, R. L., Wright, J., & Maddox, L. 2014, *AJ*, 147, 118
Riess, A. G., Casertano, S., Yuan, W., et al. 2018, *ApJ*, 861, 126
Schneider, P., Ehlers, J., & Falco, E. E. 1992, *Gravitational Lenses* (Springer-Verlag Berlin Heidelberg New York)
Scodeggio, M., Guzzo, L., Garilli, B., et al. 2018, *A&A*, 609, A84
Scolnic, D. M., Jones, D. O., Rest, A., et al. 2018, *ApJ*, 859, 101
Seikel, M., Clarkson, C., & Smith, M. 2012, *J. Cosmology Astropart. Phys.*, 6, 036
Seikel, M. & Schwarz, D. J. 2008, *J. Cosmology Astropart. Phys.*, 2, 007
Seikel, M. & Schwarz, D. J. 2009, *J. Cosmology Astropart. Phys.*, 2, 024
Shafieloo, A. 2007, *MNRAS*, 380, 1573
Shafieloo, A., Alam, U., Sahni, V., & Starobinsky, A. A. 2006, *MNRAS*, 366, 1081
Starobinsky, A. A. 1998, *Soviet Journal of Experimental and Theoretical Physics Letters*, 68, 757
Suyu, S. H., Bonvin, V., Courbin, F., et al. 2017, *MNRAS*, 468, 2590
Suzuki, N., Rubin, D., Lidman, C., et al. 2012, *ApJ*, 746, 85
Tegmark, M. 2002, *Phys. Rev. D*, 66, 103507
Wagner, J. 2017, *A&A*, 601, A131
Wagner, J. 2018a, *A&A*, 615, A102
Wagner, J. 2018b, *ArXiv e-prints* [arXiv:1809.03505]
Wagner, J., Liesenborgs, J., & Eichler, D. 2018, *ArXiv e-prints* [arXiv:1811.10618]
Wagner, J. & Tessore, N. 2018, *A&A*, 613, A6
Wang, Y. & Tegmark, M. 2005, *Phys. Rev. D*, 71, 103513
Wong, K. C., Suyu, S. H., Auger, M. W., et al. 2017, *MNRAS*, 465, 4895

Appendix A: Validity restrictions for Equation (14)

Searching for a $D_L(a, c)$ that best fits a given set of measured data at known scale factor positions a_i , $i = 1, \dots, N_D$, can be treated as a sampling problem. Since the scale factor positions belong to a limited interval, the Fourier transform of the data is limited in bandwidth. Furthermore, we assume a random, not necessarily equidistant, spacing of the a_i . Then, a generalised version of the Nyquist-Shannon sampling theorem, Landau (1967), states that the function underlying the $D_{L,i}$ can be exactly reconstructed, if the average sampling rate is (at least) twice the occupied bandwidth of the signal.

In our case, the bandwidth amounts to $2\pi(1/a_{\min} - 1/a_{\max}) \approx 15$, which is much smaller than the average sampling rate of $N_D/(a_{\max} - a_{\min}) \approx 1500$. Hence, for infinitely many coefficients c_a in Equation (14), the luminosity distance can be uniquely determined, while, in practice, the precision of the measured $D_{L,i}$ limits the number of coefficients, N_B , that can be determined.

Appendix B: Derivation of Σ_{ij}

We determine the uncertainty on $D_{L,i}$ as

$$\Delta D_{L,i} \equiv 10^{\frac{\mu + \Delta\mu_i}{5} + 1} - 10^{\frac{\mu}{5} + 1} = D_{L,i} \left(10^{\frac{\Delta\mu_i}{5}} - 1 \right), \quad (\text{B.1})$$

such that

$$\Delta D_{L,i} \Delta D_{L,j} = D_{L,i} D_{L,j} \left(10^{\frac{\Delta\mu_i}{5}} - 1 \right) \left(10^{\frac{\Delta\mu_j}{5}} - 1 \right) \quad (\text{B.2})$$

$$= D_{L,i} D_{L,j} \left(10^{\frac{\Delta\mu_i + \Delta\mu_j}{5}} - 10^{\frac{\Delta\mu_i}{5}} - 10^{\frac{\Delta\mu_j}{5}} + 1 \right). \quad (\text{B.3})$$

In order to identify $\Delta D_{L,i} \Delta D_{L,j}$ with the symmetric matrix Σ_{ij} , we symmetrise the right-hand side by identifying

$$\Delta\mu_i \equiv \frac{\Sigma_{\mu,ij}}{\sqrt{\Sigma_{\mu,jj}}} \quad \text{and} \quad \Delta\mu_j \equiv \frac{\Sigma_{\mu,ij}}{\sqrt{\Sigma_{\mu,ii}}}. \quad (\text{B.4})$$

Inserting Equation (B.4) into Equation (B.3), Equation (17) is obtained.

Appendix C: $E(a)$ for $K \neq 0$

For a given curvature $K \neq 0$, we perform the following transformations:

$$\tilde{K} = \frac{K}{|K|}, \quad \tilde{a} = \frac{a}{\sqrt{|K|}}, \quad \tilde{r} = \sqrt{|K|} r. \quad (\text{C.1})$$

Starting from Equation (11), the analogous equation to Equation (23) for $K \neq 0$ is set up in the transformed coordinates using

$$\sqrt{|K|} \int_a^1 \frac{dx}{x^2 E(x)} = \sqrt{|K|} \int_{\tilde{a}}^{\sqrt{|K|}^{-1}} d\tilde{x} \frac{dx}{d\tilde{x} |K| \tilde{x}^2 E(\tilde{x})} = \int_{\tilde{a}}^{\sqrt{|K|}^{-1}} \frac{d\tilde{x}}{\tilde{x}^2 E(\tilde{x})}, \quad (\text{C.2})$$

and

$$f_{\tilde{K}}(\tilde{r}) = \begin{cases} \sinh(\tilde{r}) & \text{for } \tilde{K} = -1 \\ \sin(\tilde{r}) & \text{for } \tilde{K} = +1 \end{cases}. \quad (\text{C.3})$$

It reads

$$\int_{\tilde{a}}^{\sqrt{|K|}^{-1}} \frac{d\tilde{x}}{\tilde{x}^2 E(\tilde{x})} = f_{\tilde{K}}^{-1} \left(\frac{H_0}{c} |K| \tilde{a} D_L(\tilde{a}) \right) \equiv f_{\tilde{K}}^{-1} \left(\tilde{a} \frac{D_L(\tilde{a})}{R_0} \right), \quad (\text{C.4})$$

in which we introduced the new scaling $R_0 = c/(H_0|K|)$. Deriving this equation with respect to \tilde{a} ,

$$-\frac{1}{\tilde{a}^2 E(\tilde{a})} = \frac{\partial f_{\tilde{K}}^{-1} \left(\tilde{a} \frac{D_L(\tilde{a})}{R_0} \right)}{\partial \left(\tilde{a} \frac{D_L(\tilde{a})}{R_0} \right)} \left(\frac{D_L(\tilde{a})}{R_0} + \frac{\tilde{a}}{R_0} \frac{dD_L(\tilde{a})}{d\tilde{a}} \right) \quad (\text{C.5})$$

and solving for $E(\tilde{a})$, we arrive at

$$E(\tilde{a}) = - \left[\tilde{a}^2 \frac{\partial f_{\tilde{K}}^{-1} \left(\tilde{a} \frac{D_L(\tilde{a})}{R_0} \right)}{\partial \left(\tilde{a} \frac{D_L(\tilde{a})}{R_0} \right)} \left(\frac{D_L(\tilde{a})}{R_0} + \frac{\tilde{a}}{R_0} \frac{dD_L(\tilde{a})}{d\tilde{a}} \right) \right]^{-1}. \quad (\text{C.6})$$

Hence, employing the transformations of Equation (C.1), we obtain $E(\tilde{a})$ as determined by Equation (C.6), in which $D_L(\tilde{a})$ is scaled by R_0 , so that we can proceed with the overall normalisation as described in Section 2.4. The subsequent steps of the method remain the same as for $K = 0$, taking into account the transformation of Equation (C.1) and $f_{\tilde{K}}$.